Impact of deformation on the atomic structures and dynamics of a Cu-Zr metallic glass: a molecular dynamics study

Y. Zhang[1], M.I. Mendelev[1], C.Z. Wang[1,2,], R. Ott[1], F. Zhang[1], M.F. Besser[1], K.M. Ho[1,2] and M.J. Kramer [1,3,*]

[1] *Ames Laboratory-USDOE, Iowa State University, Ames, Iowa 50011, USA*

[2] *Department of Physics and Astronomy, Iowa State University, Ames, Iowa 50011, USA*

[3] *Department of Materials Science and Engineering, Iowa State University, Ames, Iowa 50011, USA*

* mjkramer@ameslab.gov

Abstract

Despite numerous studies on the atomic structures of Cu-Zr metallic glasses (MGs), their inherent structural ordering, e.g., medium range order (MRO), remains difficult to describe. Specifically lacking is our understanding of how the MRO responds to deformation and the associated changes in atomic mobility. In this study, we focus on the impact of deformation on MRO and associated effect on diffusion in a well-relaxed $Cu_{64.5}Zr_{35.5}$ MG by molecular dynamics simulations. The Cu-Zr MG exhibits a larger elastic limit of 0.035 and a yield stress of 3.5 GPa. Cluster alignment method was employed to characterize the icosahedral short range order (ISRO) and Bergman type medium range order (BMRO) in the models upon loading and unloading. From this analysis, we find the disruption of both ISRO and BMRO occurs as the strain reaches about 0.02, well below the elastic limit. Within the elastic limit, the total fractions of ISRO or BMRO can be fully recovered upon unloading. The diffusivity increases 6-8 times in regions undergoing plastic deformation, which is due to the dramatic disruption of the ISRO and BMRO. By mapping the spatial distributions of the mobile atoms, we demonstrate the increase in atomic mobility is due to the extended regions of disrupted ISRO and more importantly BMRO.

I. Introduction

Compared to their crystalline counterparts, metallic glasses (MG) typically have similar elastic moduli [1] but their yield strengths are often significantly higher than their polycrystalline counter parts [2]. The unique mechanical properties of MGs have engendered considerable interest ever since their first discovery. It is widely accepted that the ultra-high strengths of MGs result from their unique atomic structures [3]. The plastic flow in MGs is usually localized at temperature well below the glass transition temperature [4], which leads to a significantly higher yield strengths in MGs. Among various MGs [5], Cu-Zr binary MGs have received enormous research interests. Firstly, binary MGs have tractable number of partial pair chemical environments for structural analysis than most MGs composed of multi-components. Secondly, Cu-Zr MGs have good glass forming abilities which allow the formation of bulk metallic glasses [6-8]. Thirdly, Cu-Zr binary and some Cu-Zr based MGs exhibit a combination of high strengths and notable plasticity[9, 10], making these alloys attractive for engineering applications. All these factors make the Cu-Zr binary alloys a good prototype model system to investigate the structure-property relationships in MGs.

A significant number of studies on the structure-property relationships in Cu-Zr binary MGs have been carried out by computer simulations [3]. Here we will briefly review the main results obtained regarding the relationship between the atomic structures and properties in Cu-Zr MGs. (1) The short range order (SRO) around Cu atoms in Cu-Zr MGs is dominated by full or distorted icosahedra (ICO) [11-17], whereas SRO around Zr atoms is mainly Frank-Kasper polyhedra [18, 19]. Different spatial organizations of ICO (i.e. vertex-, edge, face-sharing or interpenetrating ICO) have been proposed as the medium range order (MRO) [20-23]. In addition, our group has recently revealed the Bergman type MRO (BMRO) has been as another key MRO in $Cu_{64.5}Zr_{35.5}$ MGs [24]. (2) Deformation can significantly impact the density of icosahedral SRO (ISRO). Lee *et al* have reported that the mechanical properties of Cu-Zr MGs are strongly dependent on the network formed by the interpenetrating ICO [22]. A dramatic breakdown of ISRO has been demonstrated to start at the strain ε=0.07 under uniaxial loading [25]. It is also evident that the fraction of ICO inside shear bands is significantly lower than the

undeformed matrix in MGs [26, 27]. Plastic deformation or elastic deformation close to the yield stress can introduce irreversible structural change to the MGs [28-31]. (3) The atomic mobility is found to be closely related with the ICO in both Cu-Zr MGs and supercooled liquids [32]. ICO are shown to have the longest lifetime [33], lowest potential energy [34] and smallest mean squared displacements [35].

Despite the numerous studies there are still many unanswered questions regarding the structure-property relationship in Cu-Zr MGs during deformation due to the inherent challenges associated with MD studies. First, it is evident that the ultrahigh cooling rates used in molecular dynamics (MD) simulations may lead to structures which are far away from the lower cooling rates achieved in experiments. Therefore an effective approach to relax the as-quenched glassy structures is necessary. Recently it has been demonstrated that a relaxation close to the glass transition can achieve a well-relaxed glassy state using MD simulations, where the ISRO is greatly enhanced after the relaxation. [19, 36] Second, many investigations have revealed the coexistence of liquid-like and solid-like regions in Cu-Zr MGs (*i.e.* structural heterogeneity) [37-39]. Although the relationship between the structural heterogeneity and ISRO is quite clear in Cu-Zr MGs, the correlation of structural heterogeneity to MRO remains elusive. Recently the fractal nature of MGs has been suggested [40]. Nevertheless the question how to characterize the MRO that better differentiates the liquid-like and solid-like regions and establishes the correlations between atomic mobility and the MRO remains largely unexplored. Finally, it is still not clear how the deformation impacts the MRO in Cu-Zr MGs. Specific details of disruption and recovery of the SRO and MRO during loading and unloading remains unexplored.

In this work, we investigate the impact of deformation on atomic structures (in terms of ISRO and BMRO) and dynamics using an extremely well-relaxed (by MD standards) $Cu_{64.5}Zr_{35.5}$ MG model. The rest of the manuscript is organized as follows. First, we will describe the details of MD simulation and method to analyze the changes in structure during deformation. Next we will present the obtained results and discuss them. The last section will summarize our findings.

II. Methods

A. MD Models for deformation

Classical MD simulations of $Cu_{64.5}Zr_{35.5}$ MGs were performed using the Finnis-Sinclair type potential developed in Ref [32]. Isothermal-isobaric ensemble (*NPT*, *P*=0) and Nosé-Hoover thermostat were used. The time step for integration was 2.0 fs. Firstly, a cubic model with 5000 atoms (denoted as "MU") was equilibrated at 2000 K. Next this model was continuously cooled down to 700 K with a cooling rate of 10^{10} K/s. Previous study using the same potential has revealed the glass transition should occur around 750 K [24]. In order to relax the as-quenched glassy state, model MU was relaxed isothermally at 700 K for 440 ns and then further cooled to 300 K with a cooling rate of 10^{10} K/s. The model for deformation was prepared by replicating the model MU five times along the z-axis of the MD cell (denoted as "M300" in the following). The dimension of M300 (contains 25,000 atoms) was about 4.3 nm in both x- and y-directions, while the length was 21.7 nm in the z-direction. The periodic boundary conditions were removed in the z-direction (such that the final model had two free surfaces) and the velocity were randomized after which the model was equilibrated during 40 ps.

B. Details of deformation

While uniaxial loading is typically employed in experiments, exactly reproducing such a loading condition is not readily achievable in atomistic simulations. Due to the limitations of the model dimensions, effects of the exposed edges and free surfaces in MD simulations will be much more pronounced than experiments. To reduce these effects, we utilized a biaxial deformation geometry in this work. The deformation was carried out at *T*=300 K. A compressive strain in the x- and y-directions was applied at a constant strain rate of 2.0×10^{7} s^{-1}, which is typical order of magnitude used in MD simulations [25, 26, 41]. The model was deformed until the final strain of $\varepsilon_{xx}=\varepsilon_{yy}= -0.2$ ($\varepsilon_{zz}\approx0.53$). The unloading was carried out by applying a biaxial tensile strain at the same strain rate until the sum of the stress $|\sigma_{xx}+\sigma_{yy}|$ dropped to zero.

C. Structural analysis

The cluster alignment method [42] was adopted to characterize the atomic structures. A cluster around each Cu atom is extracted from the snapshot and aligned against an ideal ICO or Bergman supercluster [24] template. An ICO can be regarded as a center with twelve vertices adopting a polytetrahedral packing. The Bergman supercluster has three coordination shells with 45 atoms involved. The first shell is an ICO, surrounded by a dodecahedron as the second and another ICO as the third shell. It should be noted that the coordination shells in both the ICO and Bergman superclusters will be distorted due to different sizes of Cu and Zr atoms in Cu-Zr MGs. An alignment score is defined to describe how the as-extracted cluster deviates from the template:

$$f = \left(\frac{1}{N} \sum_{i=1}^{N} \left| r_{ic} - r_{it} \right|^2 \right)^{1/2} / r_0 \qquad (1)$$

where f is the alignment score, N is the number of the atoms in the template, r_0 is the typical bond length of the template, r_{ic} and r_{it} are the atom positions in the aligned cluster and template, respectively. The smaller the alignment score is, the more similar the structure of the cluster is to the template. We employed a cutoff alignment score of 0.146 and 0.25 to identify the ISRO and BMRO in this study, which is consistent with our previous studies [24, 36].

D. Analysis of the diffusion and dynamics

Because the diffusivity of Cu-Zr MGs under 300 K is very low, a compromise has to be made in order to investigate the atomic mobility within affordable time of MD simulations. Thus, we carried out the diffusion analysis at an elevated temperature of 600 K, which is still much lower than the glass transition temperature (750 K). Three models (all having 25,000 atoms) were employed in order to investigate the effects of deformation on the diffusion and atomic dynamics:

(1) M600: this model by heating M300 up to 600 K with a heating rate of 10^{10} K/s (and appropriate rescaling of the simulation cell in the x and y direction to provide zero pressure). No deformation is applied to this model.

(2) M600p: this model was obtained from M600 by plastic deformation at 600 K to a final strain of $\varepsilon_{xx}=\varepsilon_{yy}= -0.2$ at a strain rate of 2.0×10^{7} s^{-1}.

(3) M300p600: this model was obtained from M300 by plastic deformation at 300 K to a final strain of $\varepsilon_{xx}=\varepsilon_{yy}= -0.2$ at a strain rate of 2.0×10^{7} s^{-1}; then the model was heated to 600 K at a heat rate of 10^{10} K/s.

The mean square displacement (MSD) was calculated using the standard equation:

$$\left\langle r^2(t)\right\rangle = 1/N \sum_{i=1}^{N} \left\langle \left| r_i(t) - r_i(0) \right|^2 \right\rangle \tag{2}$$

where $r_i(t)$ and $r_i(0)$ denotes the initial and instantaneous atomic positions, respectively. <·> denotes an ensemble average over all the atoms and all initial atomic positions. The self-diffusivity (D) is calculated using the Einstein's relation:

$$D = 1/6 \lim_{t\to\infty} \partial\left\langle r^2(t)\right\rangle / \partial t \tag{3}$$

where $\langle r^2(t)\rangle$ is the MSD. The MSD was measured for about 10 ns in order to have reliable statistics. The atomic mobility was evaluated using the isoconfigurational ensemble [43]. Using M600, M600p or M300p600 as the starting structures, we adopted 1000 replicas of the system with the same initial atomic positions but different randomly assigned initial velocities. Each replica run was performed at 600K for 1 ns using *NVT* (constant number of atoms, volume and temperature) ensemble. The atomic mean square displacement ($\Delta r_{i,j}^2$) was used to evaluate the atomic mobility:

$$\Delta r_{i,j}^2 = |r_{i,j}(t=1\text{ns}) - r_{i,j}(t=0)|^2 \tag{4}$$

where $r_{i,j}(t=0)$ and $r_{i,j}(t=1\text{ns})$ are the positions of the i-th atom at the beginning and end of the j-th run, respectively. To minimize the effect of the two free surfaces perpendicular to z-axis, we ignore the atoms that have entered into the layers with distance to the free surfaces of less than 5 nm.

III. Results and discussion

A. Stress-strain curves

The stress-strain curves of the model M300 during loading and unloading are shown in Fig. 1. The loading curve clearly exhibits three stages: (1) A linear stress-strain response which corresponds to the elastic regime. The elastic limit was found to be about 0.035 and the corresponding yield stress is 3.5 GPa. (2) The next part of the loading curve corresponds to the onset of plastic flow. Following the peak stress, flow softening is exhibited with a stress drop from 3.5 GPa to 1.5 GPa in the strain range 0.035-0.06. (3) In the final part of the loading curve the flow stress keeps decreasing from 1.5GPa to 1.2 GPa as the strain exceeds 0.06. However, the rate for the stress reduction is significantly smaller than at stage (2). Upon unloading, the deformation can be fully recovered when the applied strain is lower than 0.035 (see inset in Fig. 1). An inelastic strain can be observed after the model was loaded to a strain of 0.04 and then unloaded. Pronounced inelastic strain can be clearly observed after unloading at strains larger than 0.04, indicating that the model has been plastically deformed. (The other unloading stress-strain curves can be found in supplemental materials.)

B. Structural change upon loading

Histograms of the alignment scores using ICO and Bergman supercluster as templates are present in Fig. 2. Two peaks can be seen with respect to ICO in the undeformed model on the histogram, one centered at 0.12 corresponding to the clusters having an ICO structure and the other centered at 0.2. The amplitude of the first peak shows a slight decrease when the applied strain is lower than 0.04, indicating that the change in the populations of ISRO is small. However in the strain range of 0.045-0.06, the first peak dramatically decreases, implying that the ISRO has been disrupted. With respect to Bergman supercluster, only one peak can be observed in the histogram for the undeformed model at around 0.3 with a shoulder at about 0.25. It can be seen that the amplitude of the shoulder in the histogram drops significantly when the applied strain approaches 0.04, indicating the disruption of BMRO. In comparison, there is almost no change exhibited by the ICO in the histogram at the strain of 0.04. This implies that the

BMRO is more sensitive to deformation and more prone to be disrupted than ISRO. With increasing plastic deformation, the intensity of the shoulder decreases and the main peak of the histogram shifts to a higher alignment score, indicating that the BMRO has been disrupted and the local MRO deviates from ideal distribution of Bergman supercluster during deformation.

The fractions of atoms involved in ISRO or BMRO are illustrated in Fig. 3. There are 73.5% and 51.3% atoms involved in ISRO and BMRO before deformation, respectively. The change in the fractions of atoms involved in ISRO is very small when the applied strain is below 0.02, however, a dramatic decrease in the population of ISRO from 71.9% to 52.6% takes place between the strain of 0.02 to 0.06, corresponding to the yielding and flow softening regimes on the stress-strain curve. Between 0.06 and 0.12 strain the population of ISRO decreases with a very small rate. As the strain exceeds 0.12, the fractions of atoms in ISRO approach a steady-state value of 51.4%. In contrast, the decrease in the fractions of BMRO is much more significant even within the elastic regime, i.e., from 51.3% to 40.6% as the strain increases to 0.035. The decrease becomes more drastic between 0.035 and 0.60 strain, before the atoms involved in BMRO approaches an equilibrium value of 10.0%. Two common features can be seen here: (1) both the ISRO and BMRO are disrupted most dramatically in the regime of yielding and flow softening (*i.e.* strain from 0.035 to 0.06) and (2) the populations of ISRO and BMRO fluctuate when the flow stress levels off in the plastic regime with strain larger than 0.12. The spatial distribution of the ISRO and BMRO during deformation is shown in Fig. 4 and 5, respectively. It can be seen that both ISRO and BMRO form a dense network that dominates the atomic structure before deformation. The disruption of both ISRO and BMRO during deformation is localized rather than being homogeneously distributed. Most of the ISRO remain interconnected even when the strain reaches 0.18. The deformation, however, destroys the BMRO much more significantly than ISRO, with the BMRO network starting to break-up at an applied strain of 0.05. At 0.18 strain most of BMRO becomes separated. The results clearly show that the degree of BMRO is more sensitive to the onset of plastic flow than the ISRO.

C. Dynamical disruption and recovery of ISRO and BMRO

The disruption of ISRO and BMRO shown in section 3.2 is not a static process, but rather the destruction of old ISRO and BMRO during deformation is accompanied by the generation of new ISRO and BMRO. We now focus on the dynamical disruption and recovery of ISRO and BMRO during deformation. To make the analysis clear we consider only the centers of ISRO or BMRO.

The disruption and recovery of ISRO is shown in Fig. 6, where four stages can be found: (1) No obvious change in the total fraction of ICO centers can be detected when the applied stain is below 0.015 and the disruption of old ISRO centers and generation of new ISRO centers are negligible. (2) Between the strain of 0.02 and 0.035, the total fraction of ICO centers starts to decrease upon loading and can be fully recovered upon unloading. The old or new centers of ICO are disrupted or generated at almost constant rates. However, the rate of disruption is larger than the rate of generation, resulting in a net decrease in the total fractions of ICO centers. Similar phenomena in a $Cu_{46}Zr_{54}$ MG under tension has also been reported by Lekka *et al*. [44]. Upon unloading, the total fraction of ICO centers can be almost fully recovered. Interestingly, a memory effect can be observed in this stage. Most of the newly generated ICO centers disappear and the old ICO centers in the undeformed model are recovered. (3) Between the strain of 0.035 and 0.06, the total fraction of ICO centers continuously drops at a higher rate than in stage (2). As the strain reaches 0.06 the population of ICO centers drops to about half of the undeformed model. The destruction of old centers and formation of new centers can be readily observed during loading at this stage. Meanwhile, a limited recovery can be observed upon unloading. Some of the destroyed ICO centers during loading can be restored while most of the newly generated centers will be preserved during unloading. (4) As the strain exceeds 0.08, both the rate of destruction of old ICO centers and the rate to generation of new centers decrease during loading. Therefore the total fractions of ICO centers become starts to level off. Upon unloading the recovery is negligible, indicating a irreversible structural change.

The fractions of BMRO centers upon loading and unloading are shown in Fig. 7. It can be seen that the profile of the total BMRO centers show a similar trend to the ICO

centers. However, three major differences can be clearly seen here: (1) While no obvious decrease in the total BMRO centers can be observed when the applied strain is lower than 0.02 during loading (similar to ICO centers), the disruption of the old BMRO centers and the formation of new centers can be identified as early as applied strain of 0.01. This indicates that the BMRO is much more sensitive to deformation than ISRO even within the elastic regime. (2) The total fraction of BMRO centers can be totally recovered within the elastic limit of 0.035 (also similar to ICO centers), but the destruction of old BMRO centers is permanent so that they are not recovered upon unloading. Meanwhile, the newly generated BMRO centers are preserved upon unloading. Therefore the memory effect observed in ISRO is absent for BMRO centers and indicates the need to understand the trajectory of the longer range correlations. (3) The total BMRO centers keep dropping between the strain of 0.035 and 0.06. Similar to total ICO centers, the BMRO centers reduces to about half of the undeformed model at 0.06 strain. However, the newly formed BMRO centers continue to increase in this stage upon unloading, which is qualitatively different from the behavior of ICO centers. From the strain of 0.08 to 0.18 the total populations fractions of centers fluctuate around a quarter of the undeformed model, and almost no recovery can be identified. All these results suggest that (1) the destruction of ISRO or BMRO already sets in within the elastic regime still far below yielding; (2) Statistics of both ICO centers and centers of Bergman superclusters is fully reversible within the elastic limit. However, the disruption and recovery of ISRO and BMRO coexist during loading and unloading. Therefore the elastic regime should be understood as a dynamical process; (3) Plastic flow results in an irreversible change in ISRO and BMRO in the deformed models.

D. Correlation between atomic mobility and atomic structures

The MSDs of models M600, M600p and M300p600 are shown in Fig.8. The amplitude of MSD in deformed models M600p and M300p600 is much larger than the undeformed model M600. It indicates that the atoms are more mobile in the deformed models. However, the amplitude of MSD of the two deformed models is quite similar. The diffusivity is calculated using Eq. [3] and listed in Table 1. It can be seen that the Cu diffusivity is larger than the Zr diffusivity in all the models which is consistent with

previous studies that have attributed the higher atomic mobility of Cu to its smaller atomic size relative to Zr [28, 32, 45]. It should be noted that the diffusivity of both Cu and Zr increase by 6-8 times in the deformed models compared to the undeformed model.

Intuitively, the diffusivity is dominated by the mobile atoms in MGs. To understand the enhancement of diffusion in the deformed models, we set out to identify the mobile atoms using an isoconfigurational ensemble. Firstly, we use $\Delta r_{i,j}^2$ defined by Eq. [4] to identify atomic jumps. The averaged histograms of the 1000 MD runs are presented in Fig. 9(a). The highest frequency occurs for atoms with very small $\Delta r_{i,j}^2$, indicating that the majority of the atoms only perform thermal vibrations. Starting from 0.04 nm^2, a peak emerges in the profile of the undeformed model M600. Using M600 as a reference state, we use 0.04 nm^2 as a cutoff to detect an atomic jump. An atom is put in a candidate pool for mobile atoms if it has a $\Delta r_{i,j}^2$ ≥0.04nm^2 in any MD run among the 1000 replicas. It should be pointed out that the cutoff can also be defined using the van Hove correlation functions (see supplemental materials). Similar cutoffs have also been employed by various studies [46, 47]. Secondly, we count the rate of jumps in the 1000 MD runs for each atom in the candidate pool (see Fig. 9(b)). It can be seen that most atoms in M600 only jump less than 50 times out of the 1000 MD runs, however, a long tail corresponding to the atoms that jump more frequently can be observed in the deformed models M600p and M300p600. The probability for each atom in M600 to jump among the 1000 MD runs is estimated to be 0.1%. If all the atomic jumps are assumed to be random and uncorrelated, the possibility will follow a binomial distribution $p(m)=C_{1000}^{m}(1-p)^{m}p^{m}$, where m is the rate of jumps out of the 1000 MD runs and p=0.1%. Following the binomial distribution, there should be negligibly low possibility for an atom to jump more than 150 times out of the 1000 MD runs. Therefore we define mobile atoms as the atoms that have jumped more than 150 times among the 1000 MD runs. The fractions of mobile atoms are identified to be 0.004, 0.224 and 0.240 in M600, M600p and M300p600, respectively. There are significantly more mobile atoms in the

deformed models than in the undeformed model, which is responsible for the enhancement of the diffusivity after deformation.

The results presented above raise the question how are the mobile atoms correlated with the ISRO and BMRO? To investigate this we examined the spatial distribution of mobile atoms, which is shown in Fig. 10. It can be seen that there are very few mobile atoms in the undeformed model and the ISRO or BMRO network is significantly denser than the deformed models. Instead of uniformly distributed in the model, it can be seen from Fig. 10 (a) and (b) that the mobile atoms in the deformed model tend to aggregate. Therefore the deformed models compose of regions rich in mobile or immobile atoms. Most of the atoms in ISRO or BMRO are rich in immobile atoms. From Table 1, we see only about 0.5% or 0.2% of the total mobile atoms are involved in ISRO or BMRO. Here it can be seen clearly that the atomic mobility in the deformed Cu-Zr MGs has a structural origin. Are the regions rich in mobile atoms interconnected? To reveal the spatial arrangements of the regions rich in mobile atoms, the average density of the mobile atoms was evaluated using a Gaussian smearing scheme:

$$D(r)=\frac{1}{N}\sum_{i=1}^{N}\left(\frac{\alpha}{\pi}\right)^{3/2}e^{-\alpha\left(r-r_i\right)^2} \tag{5}$$

where N is the total number of mobile atoms, $\mathbf{r}$ is the position vector of atom i, α is a constant scaling factor. Here we used α=400 nm^{-2} to perform the Gaussian smearing but the results were not very sensitive to this parameter. It can be seen from Fig. 10(c) that the regions rich in mobile atoms are not interconnected. Instead, these regions are separated by the regions rich in immobile atoms. It can be deduced that the regions rich in immobile atoms are interconnected to form a backbone of the MG. The regions rich in mobile atoms (poor in ISRO or BMRO) are embedded in the regions rich in ISRO or BMRO.

We further checked the dynamical features of the regions rich or poor in the mobile atoms using the self-part of the van Hove correlation function, which is defined by the following equation:

$$G_s(r,t)=\frac{1}{N}\left\langle \sum_{i=1}^{N}\delta\left[r_i(t)-r_i(0)-r\right]\right\rangle \tag{6}$$

where N is the total number of mobile or immobile atoms, $\mathbf{r}_i(t)$ and $\mathbf{r}_i(0)$ denote the instantaneous and initial positions of atom i, respectively. $G_s(\mathbf{r},t)$ were calculated at the time intervals of 0.1, 0.5 and 1.0 ns for both mobile and immobile atoms, respectively. It can be seen from Fig. 11 that the mobile atoms and immobile atoms show distinctly behaviors in both deformed models. The profiles of the immobile atoms have a peak centered at 0.05 nm, which show almost no change at different time intervals. It indicates that the regions rich in ISRO or BMRO have a solid-like behavior. $G_s(\mathbf{r},t)$ of the mobile atoms show a peak at 0.05 nm at a very short time interval of 0.1 ns. However, the peak is significantly broadened as time interval reaches 0.5 or 1.0 ns. Meanwhile, the positions of the peak shifts to domains with larger displacements with drastic decrease in the peak intensity. All these features indicate that the dynamics of the regions rich in mobile atoms has a liquid-like behavior [48]. It demonstrates that the liquid-like regions formed by the mobile atoms almost do not overlap with the solid-like regions formed by ISRO or BMRO. Compared to ISRO, the BMRO revealed using cluster alignment method better maps out the liquid-like and solid-like regions.

IV. Conclusions

The icosahedral short range order and Bergman-type medium range order have been unambiguously revealed using the cluster alignment method in both the undeformed and deformed Cu-Zr MGs. During loading and unloading the disruption of old ISRO or BMRO and generation of new ISRO and BMRO can be readily observed. The total fractions of ISRO or BMRO can be fully restored within the elastic limit. Nevertheless, the ISRO shows a strong memory effect where the newly formed ISRO disappear and old ISRO will restore upon unloading. Furthermore, the memory effect for BMRO is absent, where the newly formed BMRO replace the old ones being destroyed during loading. The effects of deformation can also be seen by a significant increase in diffusivity in the deformed models. The dramatic increase in the fractions of mobile atoms is responsible

for this increase in diffusivity. The deformed MGs exhibit two distinct kinds of regions: a solid-like region that is rich in ISRO or BMRO with slow dynamics and a liquid-like region that is rich in mobile atoms with fast dynamics that is depleted of ISRO or BMRO. The two kinds of regions for the most part do not overlap. From the spatial distributions the correlation of mobile atoms to BMRO is stronger and clearer than to ISRO. It should also be pointed out that the BMRO is specific to the Cu-Zr alloy modeled here; other alloys may have other topologies with which to describe their MRO. The sensitivity to other MRO to mechanical deformation remains to be investigated.

Acknowledgements

This work was supported by the U.S. Department of Energy, Office of Basic Energy Science, Division of Materials Sciences and Engineering, including the computer time allocations at the National Energy Research Scientific Computing Center (NERSC) in Berkeley, CA. The research was performed at the Ames Laboratory. Ames Laboratory is operated for the U.S. Department of Energy by Iowa State University under Contract No. DE-AC02-07CH11358.

References

[1] S. T. Liu, Z. Wang, H. L. Peng, H. B. Yu, and W. H. Wang, Scripta Mater. **67**, 9 (2012).
[2] C. A. Schuh, T. C. Hufnagel, and U. Ramamurty, Acta Mater. **55**, 4067 (2007).
[3] Y. Q. Cheng and E. Ma, Prog. Mater. Sci **56**, 379 (2011).
[4] A. S. Argon, Acta Metall. Mater. **27**, 47 (1979).
[5] A. Inoue, Acta Mater. **48**, 279 (2000).
[6] D. Wang, Y. Li, B. B. Sun, M. L. Sui, K. Lu, and E. Ma, Appl. Phys. Lett. **84**, 4029 (2004).
[7] M. B. Tang, D. Q. Zhao, M. X. Pan, and W. H. Wang, Chinese Phys.Lett. **21**, 901 (2004).
[8] D. Xu, B. Lohwongwatana, G. Duan, W. L. Johnson, and C. Garland, Acta Mater. **52**, 2621 (2004).
[9] Y. H. Liu, G. Wang, R. J. Wang, D. Q. Zhao, M. X. Pan, and W. H. Wang, Science **315**, 1385 (2007).
[10] Z. W. Zhu, H. F. Zhang, W. S. Sun, B. Z. Ding, and Z. Q. Hu, Scripta Mater. **54**, 1145 (2006).
[11] X. D. Wang, S. Yin, Q. P. Cao, J. Z. Jiang, H. Franz, and Z. H. Jin, Appl. Phys. Lett. **92**, 011902 (2008).
[12] G. Duan, D. H. Xu, Q. Zhang, G. Y. Zhang, T. Cagin, W. L. Johnson, and W. A. Goddard, Phys. Rev. B **71**, 224208 (2005).
[13] G. A. Almyras, C. E. Lekka, N. Mattern, and G. A. Evangelakis, Scripta Mater. **62**, 33 (2010).
[14] Y. Q. Cheng and E. Ma, Appl. Phys. Lett. **93**, 051910, 051910 (2008).
[15] J. Antonowicz, A. Pietnoczka, T. Drobiazg, G. A. Almyras, D. G. Papageorgiou, and G. A. Evangelakis, Philos. Mag. **92**, 1865 (2012).
[16] Z. D. Sha, Y. P. Feng, and Y. Li, Appl. Phys. Lett. **96**, 061903 (2010).
[17] Y. L. Sun and J. Shen, J. Non-cryst. Solids **355**, 1557 (2009).
[18] N. Jakse and A. Pasturel, Phys. Rev. B **78**, 214204 (2008).
[19] J. Ding, Y.-Q. Cheng, and E. Ma, Acta Mater. **69**, 343 (2014).
[20] H. W. Sheng, W. K. Luo, F. M. Alamgir, J. M. Bai, and E. Ma, Nature **439**, 419 (2006).
[21] M. Wakeda and Y. Shibutani, Acta Mater. **58**, 3963 (2010).
[22] M. Lee, C.-M. Lee, K.-R. Lee, E. Ma, and J.-C. Lee, Acta Mater. **59**, 159 (2011).
[23] R. Soklaski, Z. Nussinov, Z. Markow, K. F. Kelton, and L. Yang, Phys. Rev. B **87**, 184203 (2013).
[24] X. W. Fang, C. Z. Wang, S. G. Hao, M. J. Kramer, Y. X. Yao, M. I. Mendelev, Z. J. Ding, R. E. Napolitano, and K. M. Ho, Sci. Rep. **1**, 194, 194 (2011).
[25] A. J. Cao, Y. Q. Cheng, and E. Ma, Acta Mater. **57**, 5146 (2009).
[26] Y. Q. Cheng, A. J. Cao, H. W. Sheng, and E. Ma, Acta Mater. **56**, 5263 (2008).
[27] Y. Ritter and K. Albe, Acta Mater. **59**, 7082 (2011).
[28] Y. Zhang, N. Mattern, and J. Eckert, Acta Mater. **59**, 4303 (2011).
[29] S. C. Lee, C. M. Lee, J. C. Lee, H. J. Kim, Y. Shibutani, E. Fleury, and M. L. Falk, Appl. Phys. Lett. **92**, 151906 (2008).
[30] K. W. Park, C. M. Lee, M. Wakeda, Y. Shibutani, M. L. Falk, and J. C. Lee, Acta Mater. **56**, 5440 (2008).
[31] Y. Shi and M. L. Falk, Scripta Mater. **54**, 381 (2006).
[32] M. I. Mendelev, M. J. Kramer, R. T. Ott, and D. J. Sordelet, Philos. Mag. **89**, 109 (2009).
[33] S. G. Hao, C. Z. Wang, M. J. Kramer, and K. M. Ho, J. Appl. Phys. **107**, 053511 (2010).
[34] S. Q. Wu, C. Z. Wang, S. G. Hao, Z. Z. Zhu, and K. M. Ho, Appl. Phys. Lett. **97**, 021901 (2010).

[35] H. L. Peng, M. Z. Li, W. H. Wang, C. Z. Wang, and K. M. Ho, Appl. Phys. Lett. **96**, 021901 (2010).
[36] F. Zhang, M. I. Mendelev, Y. Zhang, C.-Z. Wang, M. J. Kramer, and K.-M. Ho, Appl. Phys. Lett. **104**, 061905 (2014).
[37] M. Li, C. Z. Wang, S. G. Hao, M. J. Kramer, and K. M. Ho, Phys. Rev. B **80**, 184201 (2009).
[38] H. Wagner, D. Bedorf, S. Kuchemann, M. Schwabe, B. Zhang, W. Arnold, and K. Samwer, Nat. Mater. **10**, 439 (2011).
[39] T. Fujita, K. Konno, W. Zhang, V. Kumar, M. Matsuura, A. Inoue, T. Sakurai, and M. W. Chen, Phys. Rev. Lett **103**, 075502 (2009).
[40] D. Ma, A. D. Stoica, and X. L. Wang, Nat. Mater. **8**, 30 (2009).
[41] M. I. Mendelev, R. T. Ott, M. Heggen, M. Feuerebacher, M. J. Kramer, and D. J. Sordelet, J. Appl. Phys. **104**, 123532 (2008).
[42] X. W. Fang, C. Z. Wang, Y. X. Yao, Z. J. Ding, and K. M. Ho, Phys. Rev. B **82**, 184204 (2010).
[43] A. Widmer-Cooper, P. Harrowell, and H. Fynewever, Phys. Rev. Lett **93**, 135701 (2004).
[44] C. E. Lekka, A. Ibenskas, A. R. Yavari, and G. A. Evangelakis, Appl. Phys. Lett. **91**, 214103 (2007).
[45] Y. L. Sun, J. Shen, and A. A. Valladares, J. Appl. Phys. **106**, 073520 (2009).
[46] M. Kluge and H. R. Schober, Phys. Rev. B **70**, 224209, 224209 (2004).
[47] C. Gaukel, M. Kluge, and H. R. Schober, J. Non-cryst. Solids **250–252, Part 2**, 664 (1999).
[48] W. Kob and H. C. Andersen, Phys. Rev. E **51**, 4626 (1995).

Figures

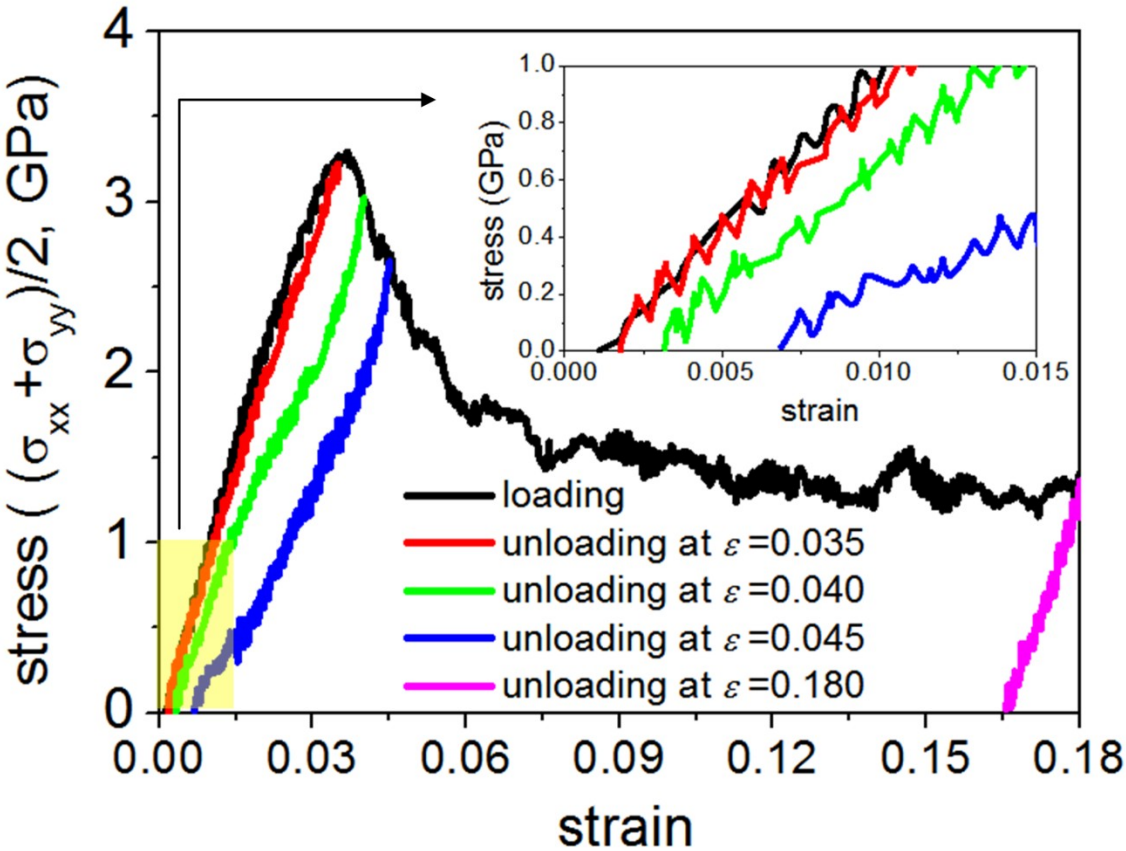

FIG. 1 The stress-strain curves (loading and unloading) of the biaxial deformation using M300 as the initial configuration. The inset shows the enlarged elastic regime, where the elastic limit is found to be 0.035.

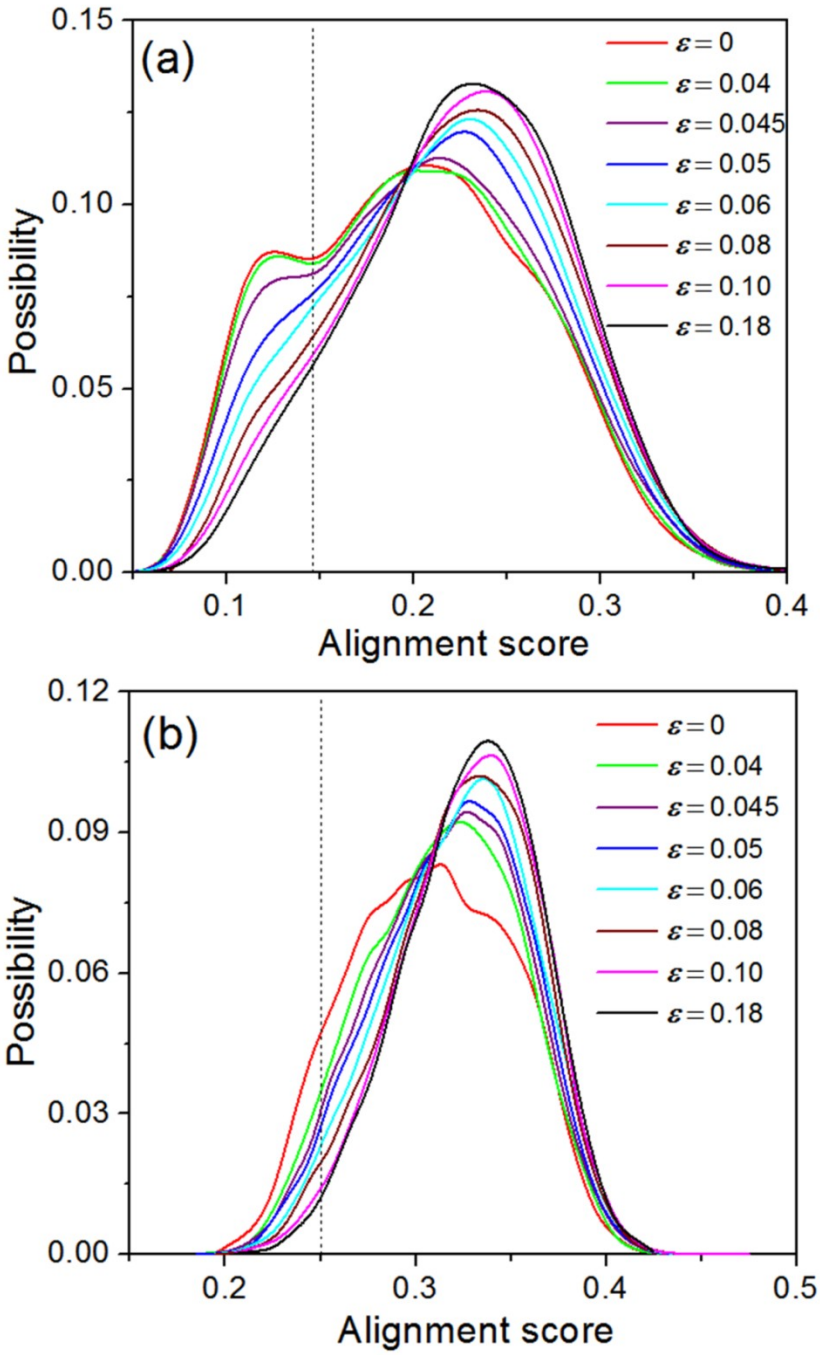

FIG. 2 Histograms of the alignment scores in the deformed models using ideal (a) icosahedra and (b) Bergman supercluster as templates. The dashed lines indicate the cutoff for ISRO or BMRO.

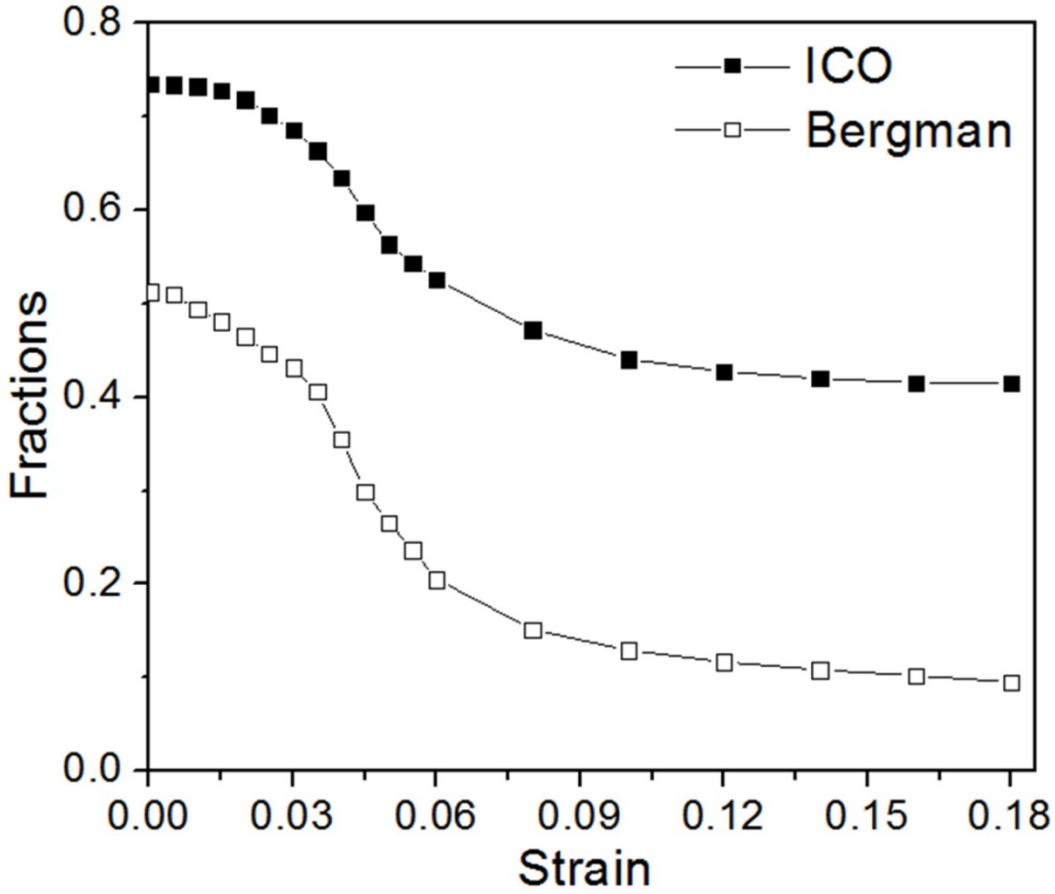

FIG. 3 The fractions of atoms involved in ISRO (solid symbols) and BMRO (open symbols) during deformation

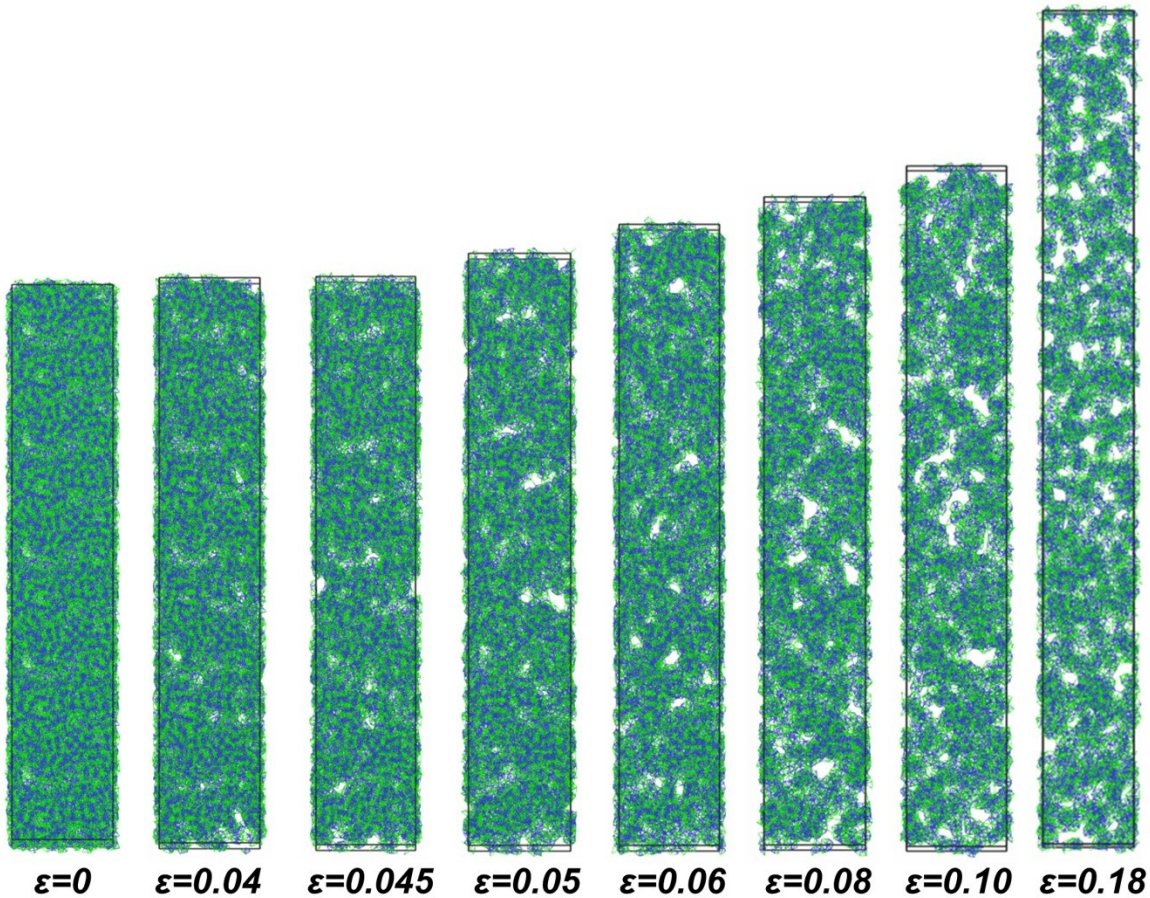

FIG. 4 Spatial distribution of the ISRO in the deformed models at various strains

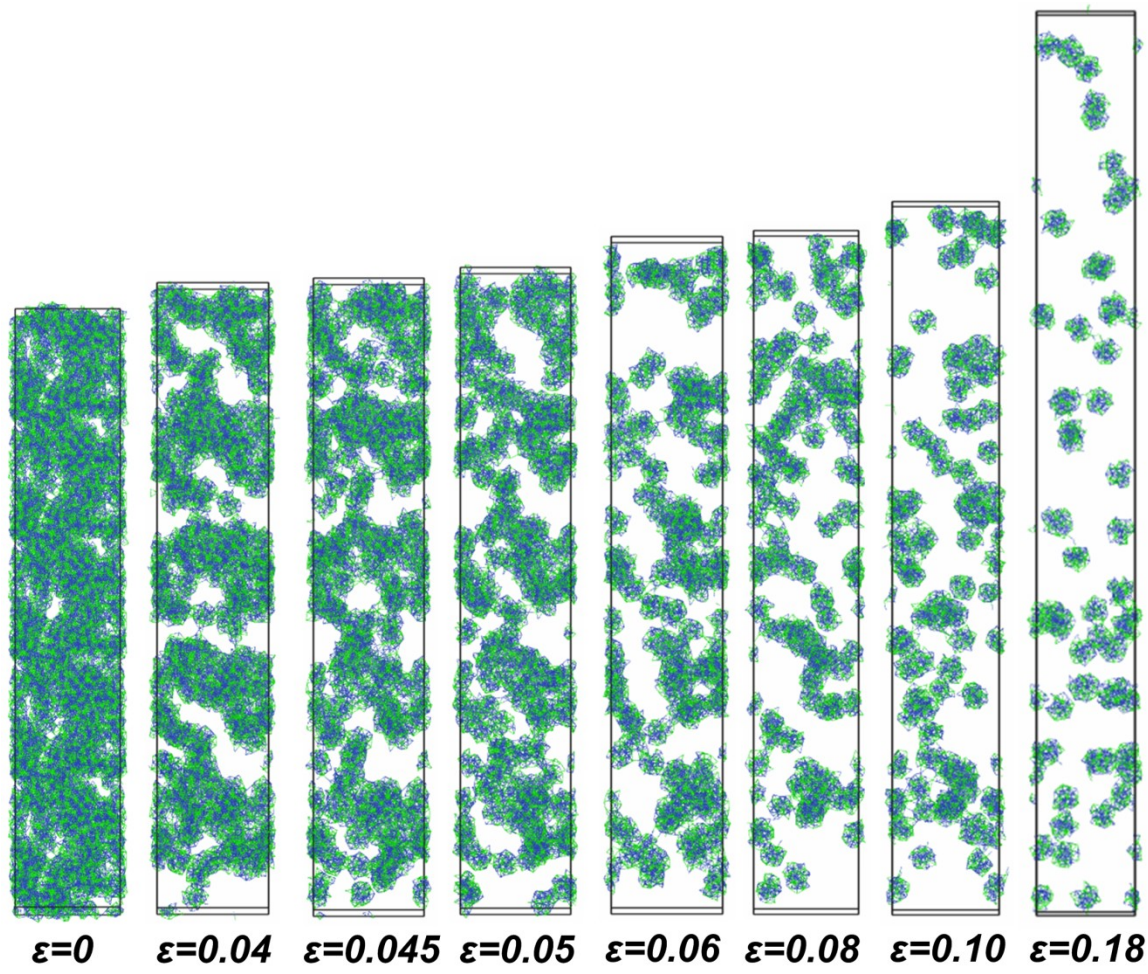

FIG. 5 Spatial distribution of the BMRO in the deformed models at various strains

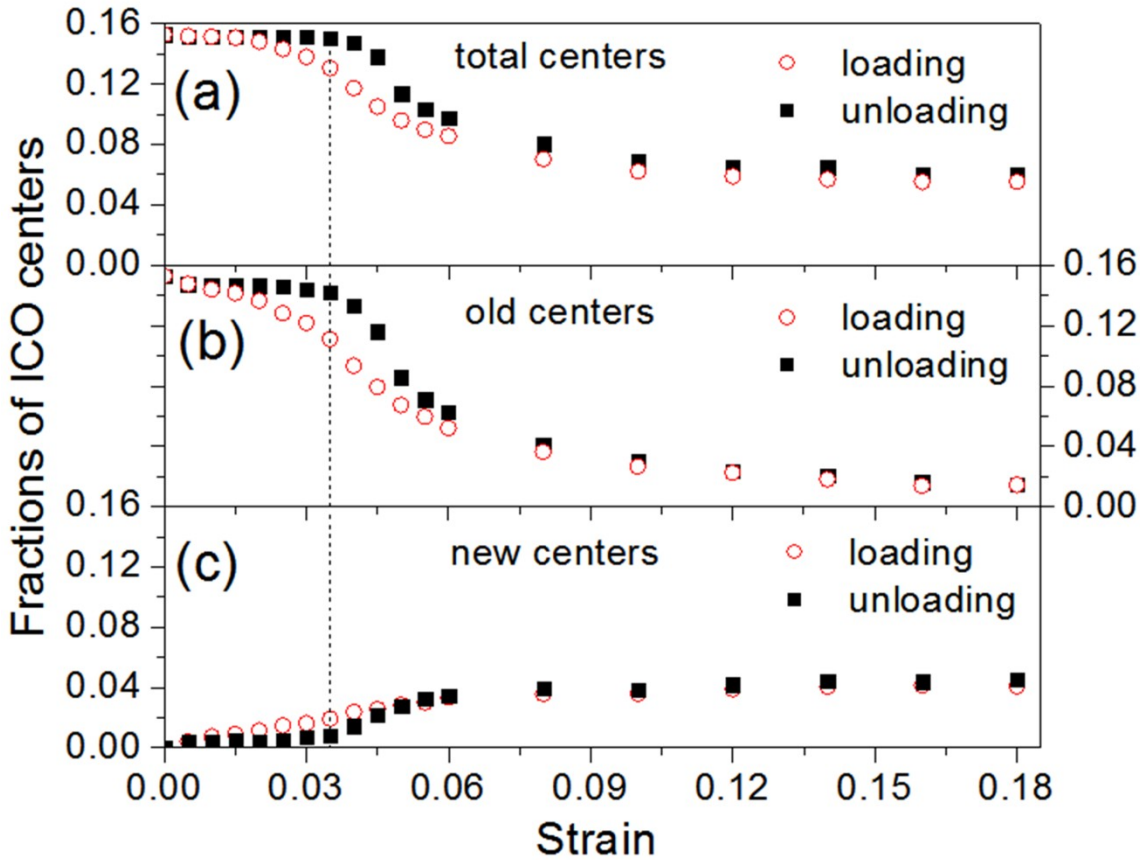

FIG. 6 Fractions of ISRO centers in the models deformed to various strains shown in the x-axis ("loading", open symbols). The deformed models were then unloaded to calculate the fractions of ISRO centers ("unloading, solid symbols). The total fractions of ISRO centers are shown in (a). Using the undeformed sample as a reference, the fraction of centers preserved in the deformed and unloaded model (denoted as "old centers") is shown in (b), while the newly formed centers in the deformed and unloaded models (denoted as "new centers") are shown in (c).

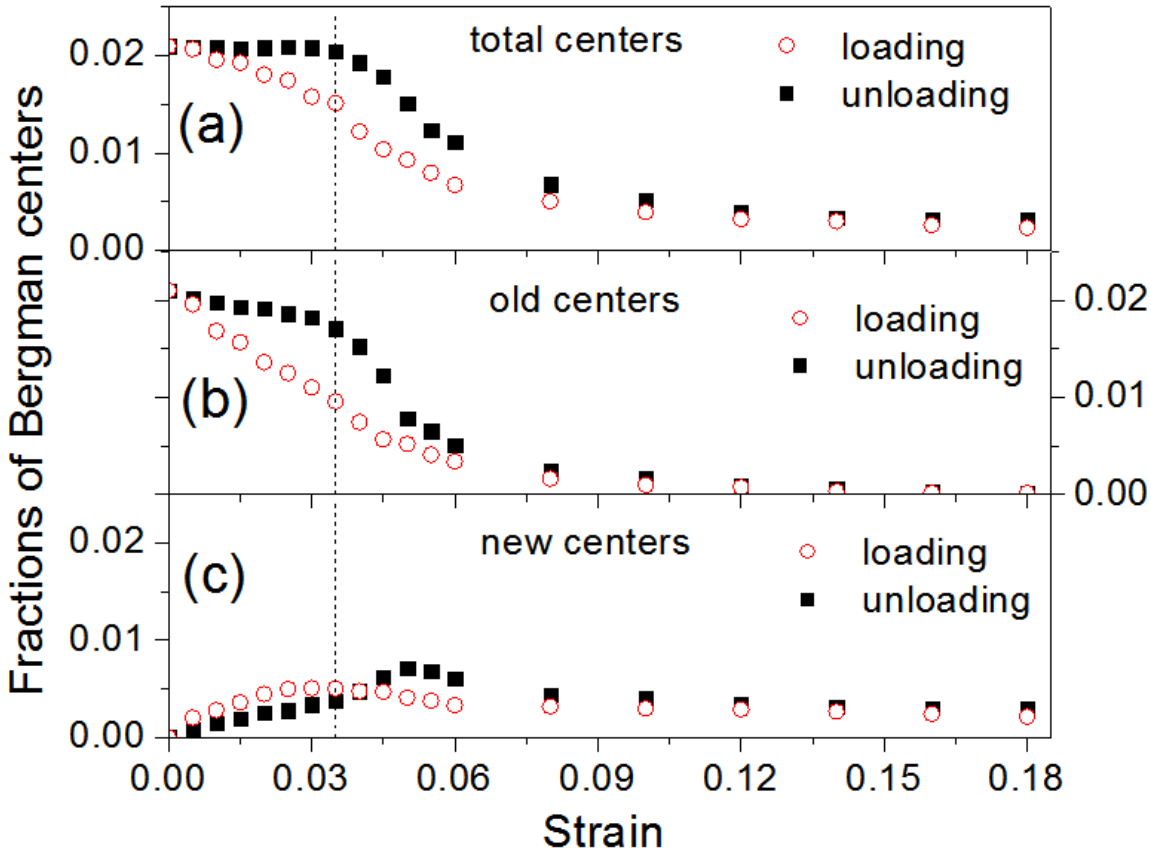

FIG. 7 Fractions of BMRO centers in the models deformed to various strains shown in the x-axis ("loading", open symbols). The deformed models were then unloaded to calculate the fractions of BMRO centers ("unloading, solid symbols). The total fractions of BMRO centers are shown in (a). Using the undeformed sample as a reference, the fraction of centers preserved in the deformed and unloaded model (denoted as "old centers") is shown in (b), while the newly formed centers in the deformed and unloaded models (denoted as "new centers") are shown in (c).

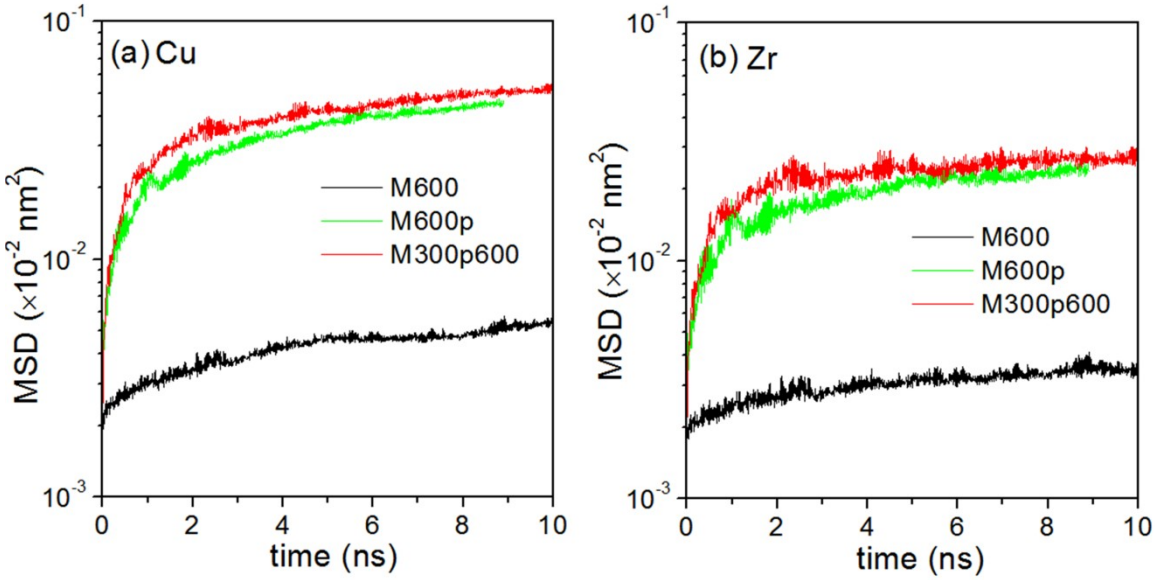

FIG. 8 Mean square displacements of (a) Cu and (b) Zr in models M600, M600p and M300p600

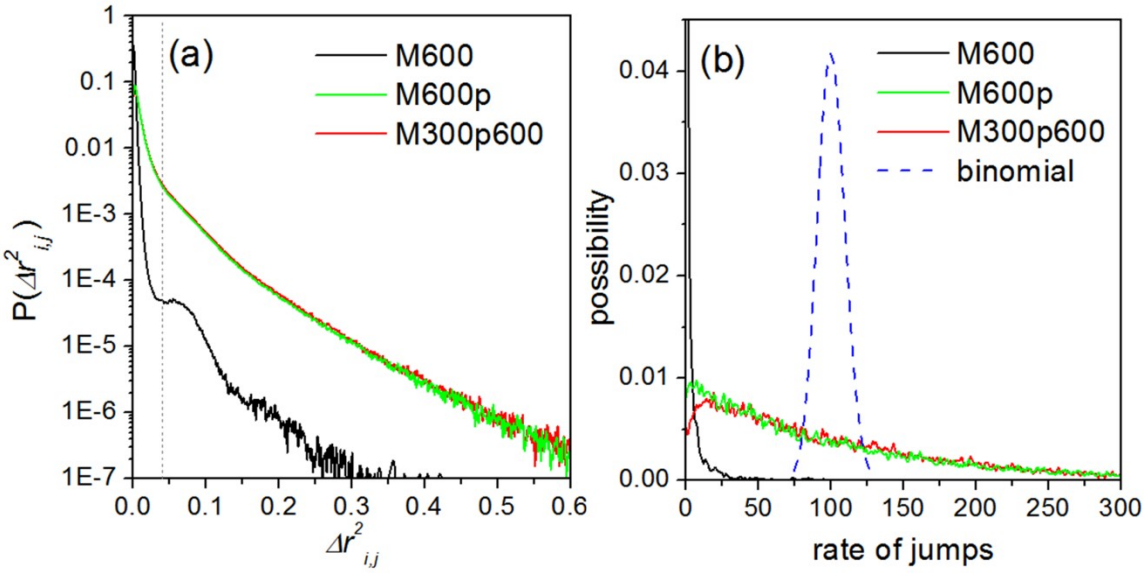

FIG. 9 Criteria to define the mobile atoms: (a) the possibility distribution of $\Delta r_{i,j}^2$ in the models M600, M600p and M300p600, the vertical solid line indicates the cutoff (0.04 nm^2) for an atomic jump; (b) the possibility distribution of rate of jumps, together with the binomial distribution for totally random and uncorrelated atomic jumps.

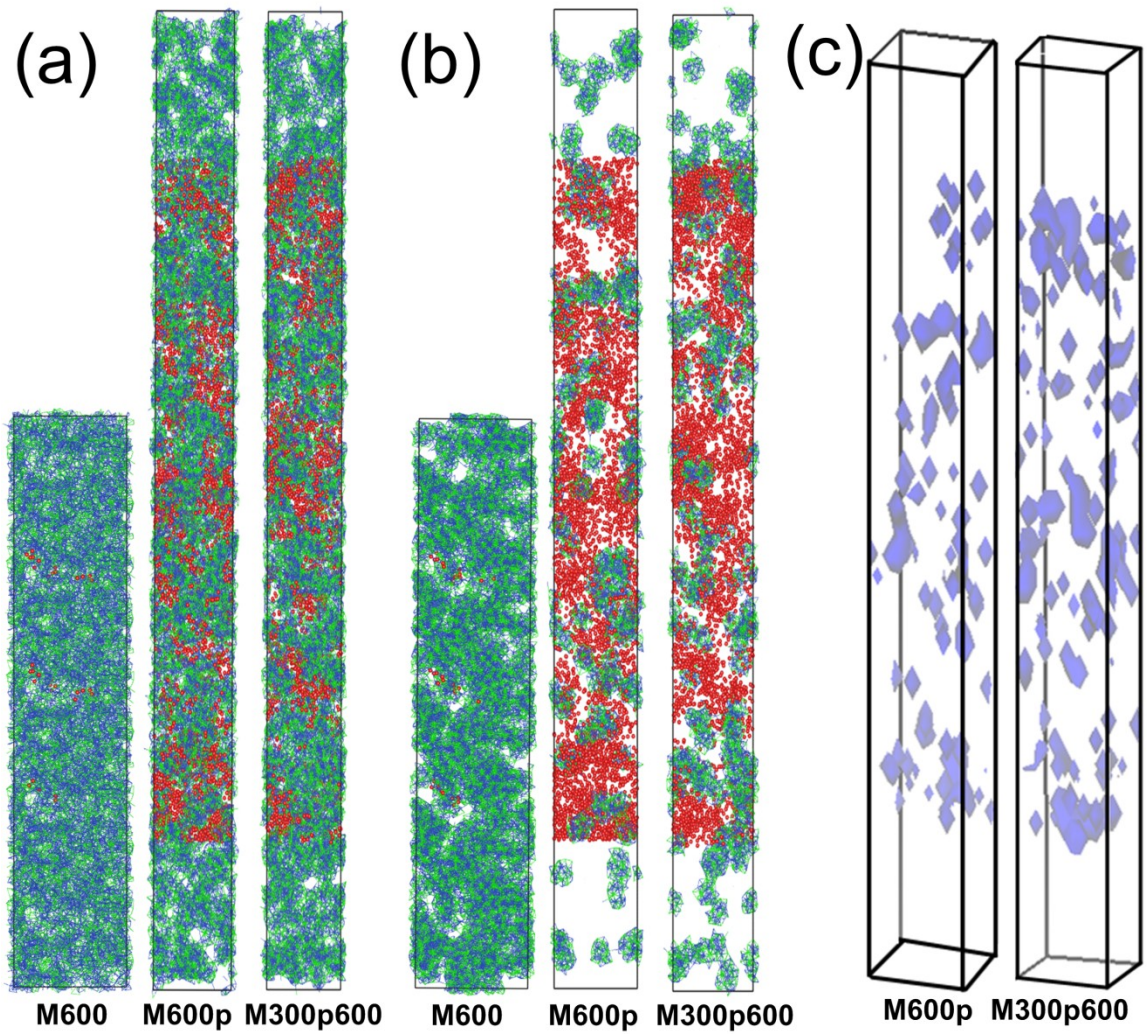

FIG. 10 Spatial distributions of the mobile atoms (in red) and the ISRO (a) or BMRO (b) networks (Cu atoms are in blue and Zr atoms are in green) in models M600, M600p and M300p600. The density of mobile atoms in M600p and M300p600 are shown by the isosurface in (c).

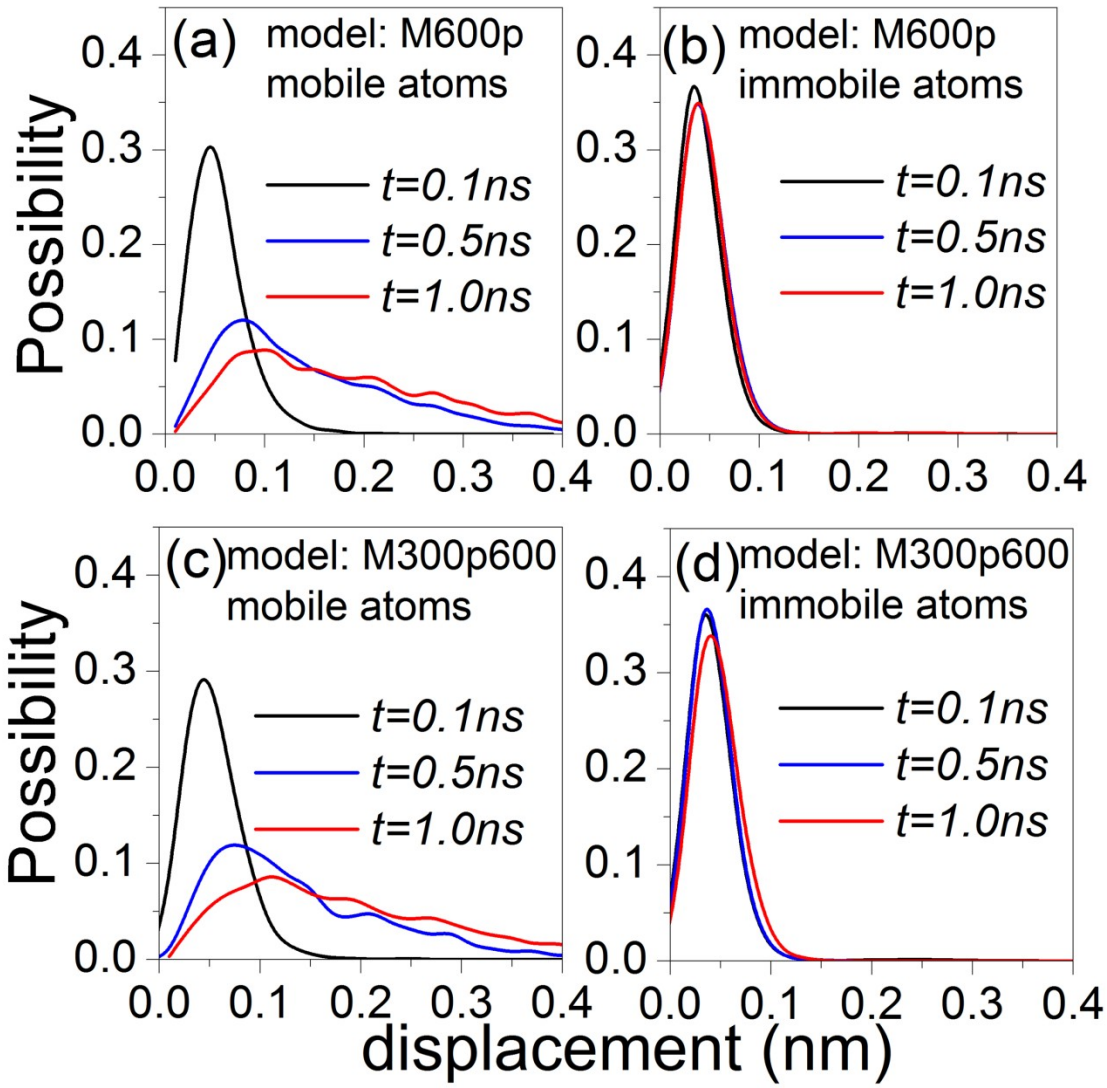

FIG. 11 The van Hove correlation functions for the mobile atoms in M600p (a) and M300p600 (b), together with the van Hove correlation functions for the immobile atoms in M600p (c) and M300p600 (d), calculated at the time interval of 0.1, 0.5 and 1.0 ns, respectively.

Table I. Self-diffusivity of Cu (D_{Cu}) and Zr (D_{Zr}), fractions of mobile atoms (f_m), fractions of mobile atoms involved in ISRO (f_{mi}) and fractions of mobile atoms involved in BMRO (f_{mb})

Model	D_{Cu} **(×10^{-9} cm^2/s)**	D**(Zr) (×10^{-9} cm^2/s)**	f_m	f_{mi}	f_{mb}
M600	0.25	0.10	0.004	0.000	0.000
M600p	1.79	0.65	0.224	0.005	0.002
M300p600	1.87	0.70	0.240	0.004	0.001